Multiple charge density wave ordering and quantum coupling of collective excitations in layered $GdTe_3$

Divya Rawat,[1] Prabir Dutta,[2] Devesh Negi,[3] Ivy Maria,[2] Surajit Saha,[3] Kanishka Biswas,[2] and Ajay Soni[1,*]

[1]*School of Physical Sciences, Indian Institute of Technology Mandi, Mandi 175005, Himachal Pradesh, India*

[2]*New Chemistry Unit, International Centre of Materials Science, and School of Advanced Materials, Jawaharlal Nehru Centre for Advanced Scientific Research, Bangalore 560064, Karnataka, India*

[3]*Department of Physics, Indian Institute of Science Education and Research Bhopal, Bhopal 462066, Madhya Pradesh, India*

(Received 24 June 2024; accepted 12 August 2024; published 27 August 2024)

Rare-earth tritellurides represent quasi-two-dimensional systems that exhibit multiple charge density wave (CDW) transitions alongside magnetic ordering. However, the interplay between the phonon dynamics of collective excitations and local magnetism remains unclear. $GdTe_3$ is an interesting material having an incommensurate CDW (ICDW), at $T_{ICDW} \sim 380$ K, an antiferromagnetic transition at $T_N \sim 13$ K, and with an expectation of another CDW ordering. We emphasize electron-spin-phonon and mode coupling in $GdTe_3$ through temperature dependent Raman spectroscopy complemented by heat capacity and magnetization measurements. Disappearance of zone-folded mode (Z^*) and observed coupling behavior of amplitude mode suggest the existence of another ordering at ~240 K, in addition to known ICDW. By employing phonon renormalization, we estimated significant strength of spin-phonon coupling, ($\lambda_{s-ph} \sim 0.234$) and accentuated on the phonon dynamics associated with CDW instabilities in $GdTe_3$.

DOI: 10.1103/PhysRevB.110.075155

I. INTRODUCTION

Electron correlations play a remarkable role in the study of quantum multibody phenomena such as charge density wave (CDW), superconductivity, topological surface states, and magnetism. The exchange correlations among the electrons and phonons can enhance the electron-electron (*e-e*), electron-phonon (*e-ph*), and spin-phonon (*s-ph*) coupling, which can lead to the coexistence of multibody quantum phenomena in materials [1–3]. CDW is one such example, which can be understood based on the one-dimensional Peierls instabilities. Here, the periodic modulation of electronic charge density (ρ) can be written as $\rho = \rho_0 + \rho_1 \cos(q_0 r + \varphi)$, where ρ_0 is the unmodulated electronic charge density, and ρ_1 and φ are the amplitude and phase factor of the CDW, respectively [4]. The CDW instabilities are conventionally related with Fermi surface nesting (FSN), where segments of the Fermi contours are connected by CDW wave vector ($\boldsymbol{q}_{CDW}$) and leads to the opening of the band gap (Δ_{CDW}) at the Fermi surface. However, it is asserted that FSN may not be the exact mechanism behind the origin of CDW instability, as revealed by several experimental observations of inelastic x-ray scattering, angle resolved photoemission spectroscopy (ARPES), and Raman spectroscopy [5–7]. Additionally, for two-dimensional chalcogenides the CDW instabilities are primarily driven by the *e-ph* coupling with the reconstruction of reciprocal lattice unit cell and modified Brillouin zone (BZ) [8–10]. Based on the reconstructions, CDW can be distinguished as incommensurate (ICDW) and commensurate (CCDW) CDW, where $\boldsymbol{q}_{CDW}$ is a nonintegral and an integral multiple of the reciprocal lattice vector of the undistorted lattice, respectively [7]. The lattice reconstruction modifies the electronic band structure and folds the boundary of the BZ, which enhances the possibilities of the emergence of collective (amplitude and phase modes) and zone-folded (ZF) modes [11]. The collective modes are mainly associated with the oscillation of the amplitude and phase of the CDW order parameter, while ZF modes originate from the modified electronic band structure which can couple to the electronic density at the $\boldsymbol{q}_{CDW}$ [12]. The impact of electronic charge and lattice ordering on CDWs is well understood in terms of ICDW, CCDW, and the appearance of collective excitations. However, the influence of the spin of magnetic atoms, in CDW materials, on the dynamics of collective excitations remains unaddressed yet.

Rare-earth tritellurides (RTe_3) are fascinating materials for studying the underlying physics of CDW and its correlation with magnetism. The intriguing crystal structure of RTe_3 is composed of Te square-net sheets separated by double-corrugated RTe slabs [Fig. 1(a)] [13–15]. The CDW instabilities in RTe_3 mainly appear at quite high temperatures (above ~244 K) and are driven by FSN, which has been observed from ultrafast spectroscopy, electron diffraction, transport measurements, and ARPES [5,15,16]. Generally, RTe_3 with heavier R atoms (Tm, Er, Ho, Dy) exhibits two CDW transitions, while the one with lighter R (La, Gd, Ce, Tb) undergoes only one [15,17–20]. The ARPES measurements on RTe_3 suggest that the first CDW transition appears because of imperfect nesting of the Fermi surface, while the remaining nesting can lead to a second CDW transition at lower temperatures [5]. Additionally, the excitation of low energy phonons, associated with the heavier R elements, can drive more than one CDW ordering [21]. Among the vast family of RTe_3, the $GdTe_3$ has gained significant attention

*Contact author: ajay@iitmandi.ac.in

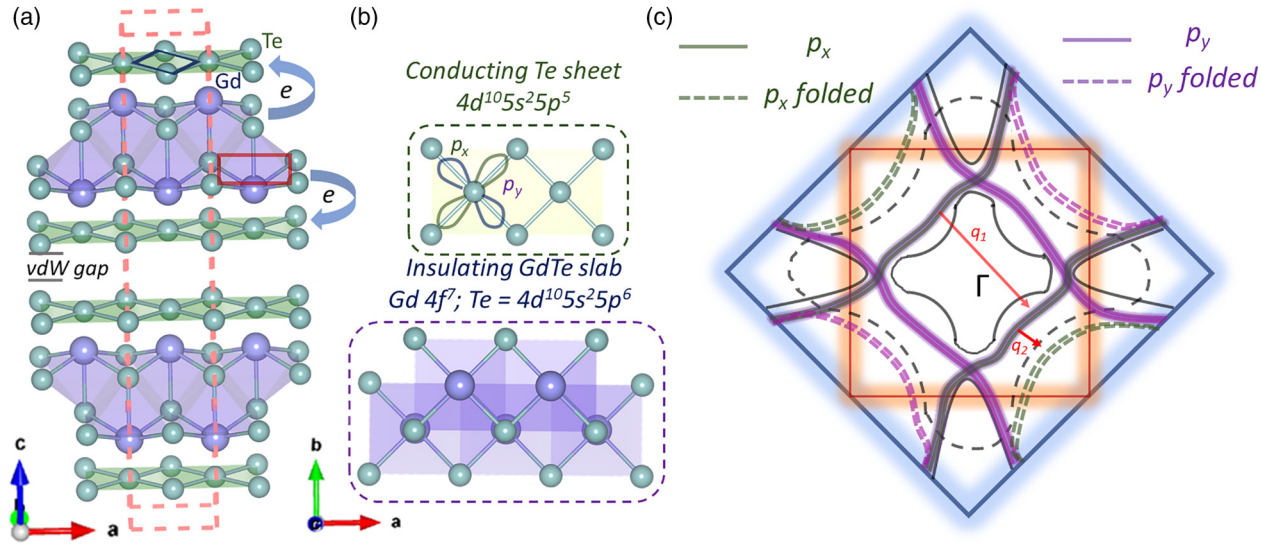

FIG. 1. Schematics of (a) crystal structure of layered $GdTe_3$, and (b) top view of conducting square Te sheet and insulating GdTe slab on *ab* plane. The red dashed line is to guide the eye to the unit cell. Gd and Te atoms are labeled in purple and green color. (c) Schematic of Fermi surface in 3D and 2D BZ formed by a corrugated GdTe slab and Te-square net sheets, respectively [20,25]. The electronic states near Fermi energy are mainly dominated by p_x and p_y orbitals of Te. The red arrow represents the nesting vector corresponding to q_{CDW1}.

because of interesting CDW with multiple gap openings at ∼480 and ∼270 meV, a high mobility (39 000 $\mathrm{cm^2\,V^{-1}\,s^{-1}}$ at 2 K, and believed to exhibit only one ICDW at, $T_{\mathrm{ICDW}} \sim$ 380 K (corresponding to $\Delta_{\mathrm{CDW}} \sim 480$ meV), and an antiferromagnetic (AFM) transition at $T_N \sim 13$ K [22–24]. The transition temperature corresponding to $\Delta_{\mathrm{CDW}} \sim 270$ meV is still elusive and requires further investigation.

Here, low temperature Raman spectroscopy combined with heat capacity and magnetization measurement are performed to study the multibody interactions and the phonon dynamics of collective excitations. The results significantly advance the understanding of quantum coupling, identifies different ordering, and provides a comprehensive phase diagram delineating different temperature regions to explore the complex phase behavior of $GdTe_3$. Our results reveal a possible ordering near ∼240 K, besides the T_{ICDW} at ∼380 K, and also highlight the significant *s-ph* coupling owing to the long-ranged AFM ordering.

II. EXPERIMENT

A high quality polycrystalline sample of $GdTe_3$ was synthesized by the melt-grown method [25]. Raman spectroscopy was performed using a Horiba Jobin-Vyon LabRAM HR Evolution Raman spectrometer equipped with Czerny-turner grating (1800 grooves/mm), 50*X* long working distance objective (NA ∼ 0.75), 633-nm laser excitation with Peltier cooled charge-coupled device detector. An ultralow frequency filter was used to access the low-frequency Raman modes. All the experimental conditions (acquisition ∼50 sec, single accumulation, laser power <1 mW) have been kept fixed throughout the experiments. Raman spectroscopy at low temperature was done using a Montana cryostat under inert atmosphere in the temperature range 3–340 K. All the experiments were done in vacuum atmosphere since $GdTe_3$ oxidizes easily in ambient conditions. All the spectra have been fitted by the Lorentzian and Breit-Wigner Fano function (BWF) to evaluate the phonon frequency (ω), full width at half maximum (Γ), and integrated area (IA) of the Raman modes. The temperature dependence of dc magnetization (M) was performed in a Quantum Design superconducting quantum interference device magnetometer with applied field $H =$ 100 Oe. The low temperature heat capacity (C_{p}) was measured in a DynaCool Physical Property Measurement System (PPMS, Quantum Design).

III. RESULTS AND DISCUSSION

Layered $GdTe_3$ has an orthorhombic crystal structure (*Cmcm* space group) with double corrugated insulating GdTe slabs sandwiched between two conducting Te square net sheets, stacked along the *c* axis and separated by weak van der Waals force [Fig. 1(a)]. The dominant electronic states near the Fermi energy (E_{F}) are mainly composed of $5p_x$ and $5p_y$ orbitals of Te as shown in Fig. 1(b). The interlayer coupling between the two conducting Te sheets causes a splitting of the Fermi surface by breaking the degeneracy of the conduction band [25]. In literature, the Fermi surface map of the $GdTe_3$ has been investigated using ARPES and first-principle density functional theory, where additional folded bands have been observed in the reduced three dimensional (3D) BZ arising from the bands in the 2D BZ [17,20,25]. Owing to the interesting Fermi surface, $GdTe_3$ has FSN at $q_{\mathrm{CDW_1}}$ (0.36, 0.36, 0) and $q_{\mathrm{CDW_2}}$ (0.11, 0.11, 0) [25]. Figure 1(c) shows the schematic of 3D and 2D BZ of $GdTe_3$ formed by the GdTe slab [red rectangle in Fig. 1(a)] and Te sheet [blue rectangle in Fig. 1(a)] [20,25]. $GdTe_3$ exhibits ICDW at $T_{\mathrm{ICDW}} \sim 380$ K, observed from the transport measurement and AFM transition at $T_N \sim 13$ K, respectively [23,25].

From the group theoretical calculations, the irreducible representation (χ) of all Raman active modes of $GdTe_3$ can

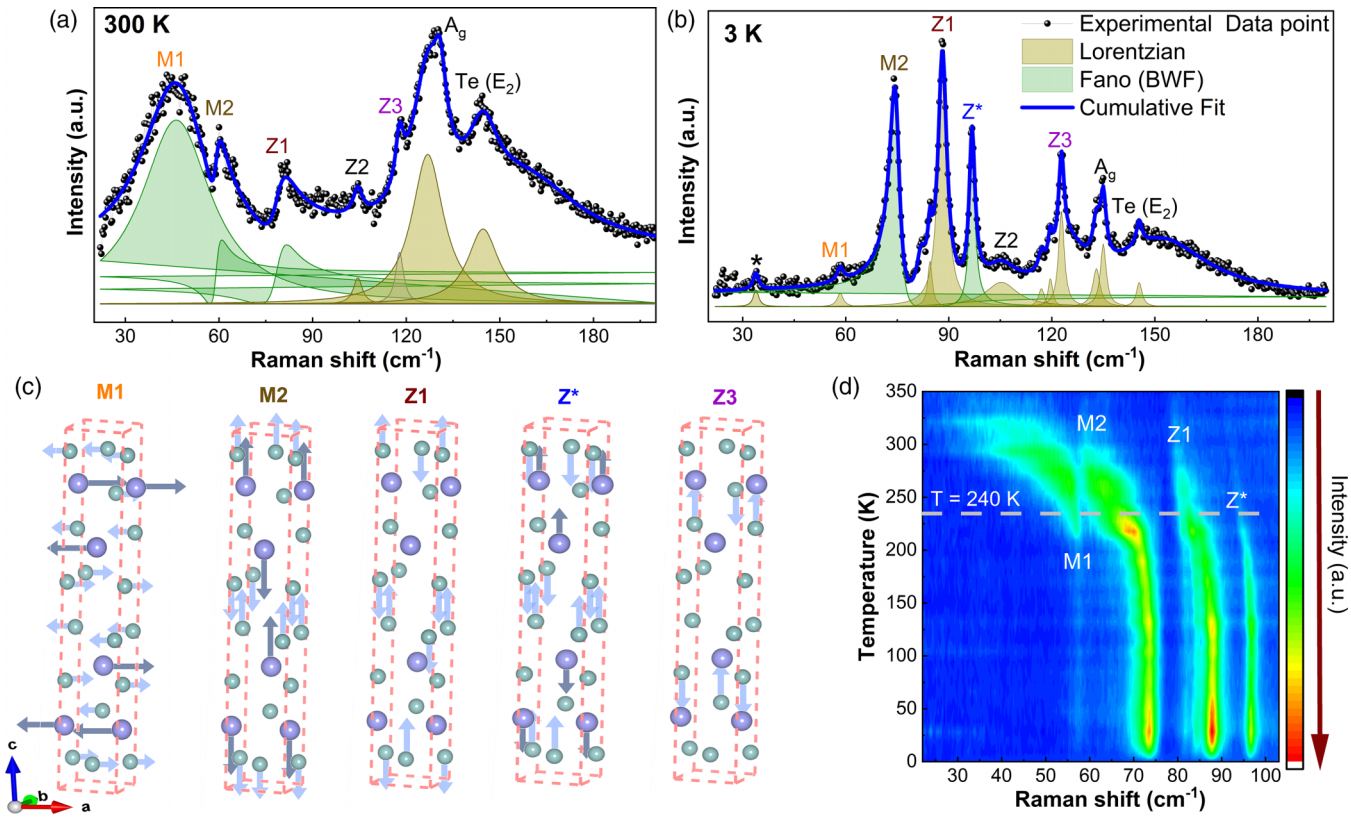

FIG. 2. Raman spectra of $GdTe_3$ (a) at 300 K and (b) at 3 K showing amplitude ($M1$ and $M2$), zone-folded ($Z1$, Z^*, $Z2$, and $Z3$) and characteristic mode [A_g and Te (E_2)]. (c) Schematic displacements of Gd and Te atom associated with $M1$, $M2$, $Z1$, Z^*, $Z3$. (d) Temperature dependent intensity map of $M1$, $M2$, $Z1$, and Z^*. The Raman intensities of all modes are strongly enhanced below ~240 K except $M1$.

be given as $\chi = 4A_g + 4B_{1g} + 4B_{3g}$ [22]. Figure 2(a) shows the Raman spectra of $GdTe_3$ at 300 K ($< T_{ICDW}$) consisting of the modes at ~45 cm^{-1} ($M1$), ~60 cm^{-1} ($M2$), ~81 cm^{-1} ($Z1$), ~104 cm^{-1} ($Z2$), ~118 cm^{-1} ($Z3$), ~129 cm^{-1} (A_g), and ~145 cm^{-1} (E_2). The low ω modes (<100 cm^{-1}) have a major contribution from the Gd of the GdTe slab and Te atoms of the sheets; on the other hand, the Te of the GdTe slab contributes to the modes above ~100 cm^{-1} [25]. Here, the $M1$ and $M2$ are amplitude (AMP) modes, while $Z1$, $Z2$, and $Z3$ are zone folded (ZF) modes originating from the reconstructed lattice below T_{ICDW} [6,19]. Both the AMP and ZF modes exhibit an asymmetric Fano line shape, and their analysis suggests the involvement of *e-ph* interactions in $GdTe_3$ even at 300 K [26]. Hence, both the Lorentzian and Breit-Wigner-Fano functions have been used for the fitting of symmetric and asymmetric line shapes, respectively [9]. Figure 2(b) shows the Raman spectra at 3 K, which consists of modes at ~36 cm^{-1}, ~58 cm^{-1} ($M1$), ~74 cm^{-1} ($M2$), ~88 cm^{-1} ($Z1$), ~97 cm^{-1} (Z^*), ~106 cm^{-1} ($Z2$), ~123 cm^{-1} ($Z3$), ~135 cm^{-1} (A_g), and ~145 cm^{-1} [Te(E_2)]. The symmetry assignments, with literature comparison, of all observed Raman active modes are elaborated in Table SI of Supplemental Material (SM) [22,25,27]. The atomic displacements associated with AMP ($M1$ and $M2$) and ZF ($Z1$, Z^*, and $Z3$) modes of $GdTe_3$ are presented in Fig. 2(c). The atomic displacements of all modes are shown along the z axis, except for $M1$, which is along the y axis. The $M1$, $M2$, and Z^* involve atomic displacements of both Gd (from the GdTe slab) and Te (from the Te sheet) atoms. In contrast, $Z1$ and $Z3$ only involve atomic displacements of Te atoms from the sheet and slab, respectively. Compared to 300 K, all observed modes are blueshifted and have higher intensity at 3 K, except $M1$. Additionally, two extra modes, ~97 cm^{-1} (Z^*) and ~36 cm^{-1}, have been observed at 3 K. While the Z^* mode corresponds to ZF modes, but the origin of ~36 cm^{-1} is not clear yet. To elucidate the phonon dynamic of these collective modes, detailed temperature dependent Raman studies have been performed from ~3 to ~340 K (Fig. S1 of the SM [27]). Figure 2(d) shows the Raman intensity color map of $M1$, $M2$, $Z1$, and Z^*, where the horizontal axis, vertical axis, and color scale correspond to the Raman shift, temperature, and Raman intensity, respectively. As temperature approaches T_{ICDW} ~ 380 K, significant changes, such as (i) anomalous softening and broadening of AMP and ZF modes, (ii) disappearance of Z^* at ~240 K, and (iii) Fano line shape of AMP and ZF modes, are clearly evident in Fig. S1 of the SM [27].

Temperature variation of phonon frequency [$\omega(T)$] of the AMP and ZF modes have been shown in Fig. 3(a). With increase in the temperature, the $\omega(T)$ of $M1$ remains constant while $M2$ exhibits softening until ~240 K. Beyond ~240 K, $M1$ starts to soften dramatically, whereas the $\omega(T)$ of $M2$ remains constant. The $\omega(T)$ of $Z1$ also exhibits a similar variation to that of $M2$ until ~240 K, followed by a change in slope above ~240 K. On the other hand, the $\omega(T)$ of Z^* and $Z3$ exhibit the usual softening. The unusual phonon dynamics of $M1$, $M2$, and $Z1$ indicate a possible

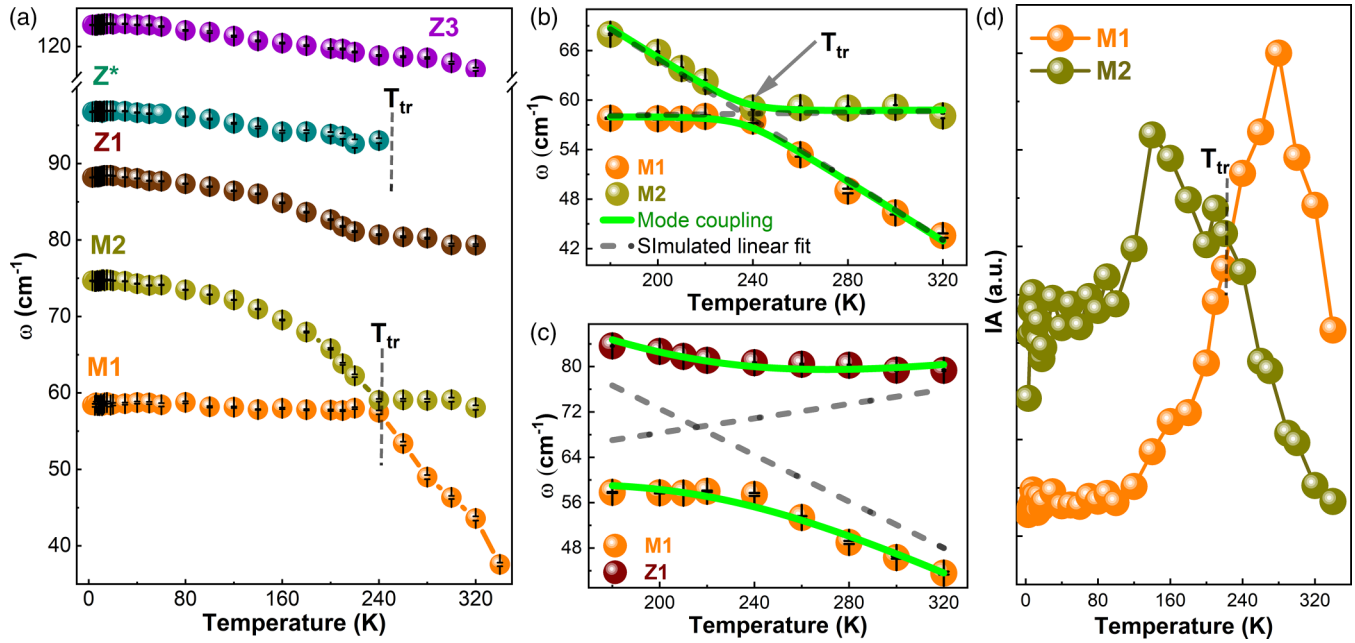

FIG. 3. The $\omega(T)$ of $M1$, $M2$, $Z1$, Z^*, and $Z3$ (a) from 3 to 340 K. The expanded view of $\omega(T)$ in between 180 and 320 K for (b) $M1$ and $M2$, and (c) $M1$ and $Z1$. Here, the solid green line represents the fitting of the mode using the equation for the coupling excitation and dashed grey line is the simulated linear curve, when they are uncoupled. (d) The temperature variation of integrated area of $M1$ and $M2$ for $GdTe_3$.

coupling among the modes and the existence of some ordering, which needs to be analyzed in detail. Similar to $GdTe_3$, the signatures of mode coupling of AMP modes have also been observed in $DyTe_3$ and $LaTe_3$ [6]. With the considerations of two coupled oscillator model, the renormalized frequency of the coupling modes can be defined by $\omega^{\pm} = \frac{1}{2}[(\omega_1 + \omega_2) \pm \sqrt{(\omega_1 + \omega_2)^2 - 4(\omega_1\omega_2 - V^2)}]$. Here, V is the coupling strength between the modes, $\omega_1(+)$ and $\omega_2(-)$ are the uncoupled mode frequencies, which are approximated to be linear, $\omega_1 = \omega_1(0) + AT$ and $\omega_2 = \omega_2(0) + BT$, where A and B are the slopes of the mode frequency [28]. The $\omega(T)$ of $M1$ and $M2$ are fitted in the temperature range 180–320 K [Fig. 3(b)], with the coupling equation, which indicates that these two modes are strongly coupled with each other at ∼240 K. Despite being far from $M1$, the $Z1$ also appears to couple strongly with $M1$, as shown in Fig. 3(c). The fitted parameters from the mode coupling of $M1$ and $M2$ ($M1$ and $Z1$) are extracted and mentioned in Table SII of the SM, where the coupling strength V is higher for $Z1$ (∼11.93 cm^{-1}) than $M2$ (∼1.34 cm^{-1}) [27]. Further, the temperature variation of $\Gamma(T)$ [Fig. S2(a) of the SM [27]] and IA(T) [Fig. 3(d)] of $M1$ and $M2$ also has a crossover at ∼240 K. As the temperature increases, the IA of both $M1$ and $M2$ remains almost constant up to ∼160 K. However, for temperatures above ∼ 160 K, the IA of $M1$ increases while it decreases for $M2$, and they share the same spectral weight around ∼240 K. For $T > 240$ K, the $M2$ transfers its spectral weight to $M1$, and both vanish near T_{ICDW}, also confirming the coupling behavior of $M1$ and $M2$ at ∼240 K. In addition, Z^* disappears at ∼240 K, confirming that there is a structure ordering that occurs at ∼240 K. The temperature at which Z^* disappears, around ∼240 K, along with the coupling behavior of $M1$, $M2$, and $Z1$, can be interpreted as the transition temperature (T_{tr}) for another ordering below T_{ICDW}. As discussed in the literature, multiple band gaps $\Delta_{CDW} \sim 480$ meV (corresponding to T_{ICDW}) and $\Delta_{CDW} \sim 240$ meV (with unknown temperature) exist on the Fermi surface of $GdTe_3$, at different temperatures. The temperature range for the existence of $\Delta_{CDW} \sim 240$ meV is found between 100 and 200 K [21]. Therefore, based on our analysis, we are of the opinion that $T_{tr} \sim 240$ K is the temperature corresponding to another possible CDW ordering below 380 K in $GdTe_3$.

Figure 4(a) shows the low temperature heat capacity [$C_p(T)$] and magnetizations [$M(T)$] measurements. Here, low-temperature $C_p(T)$ shows two transitions at $T \sim 6$ K and ∼13 K, which makes the system more interesting. Guo *et al.* [23] have observed another AFM-like feature for $GdTe_3$ single crystal in $C_p(T)$ at ∼9 K, which however is not observed in our case because of the polycrystalline nature of the sample. The change in entropies (S) at both transitions have been estimated, S_1 (∼8.83 J/mol K) and S_2 (∼6.08 J/mol K) corresponding $T \sim 6$ K and $T \sim 13$ K, respectively and magnetic entropy ($S_{mag} \sim 12.42$ J/mol K) are shown in Fig. S3 of the SM [27,29]. From the $M(T)$, the transition at $T_N \sim 13$ K is clearly an AFM transition because of the long-range AFM ordering arising from the magnetic interaction of Gd^{+3} ions, via superexchange interactions within the insulating GdTe slab. Additionally, there is also a slight magnetic contribution from conduction electrons (of Te in the Te sheet) through Ruderman-Kittel-Kasuya-Yosida (RKKY) interactions [20]. The Weiss temperature ($\theta \sim -13.65$ K) and effective magnetic moment ($\mu_{eff} \sim 7.85\mu_B$/f.u.) have been estimated from the magnetic data, as shown in Fig. S4 of the SM [27]. The magnetic ordering induces phonon renormalization, $\Delta\omega = \omega(T) - \omega_0(T)$, which is proportional to spin-spin correlation function $\langle S_i \cdot S_j \rangle$ i.e, $\Delta\omega \approx \lambda_{s-ph}\langle S_i \cdot S_j \rangle$, where

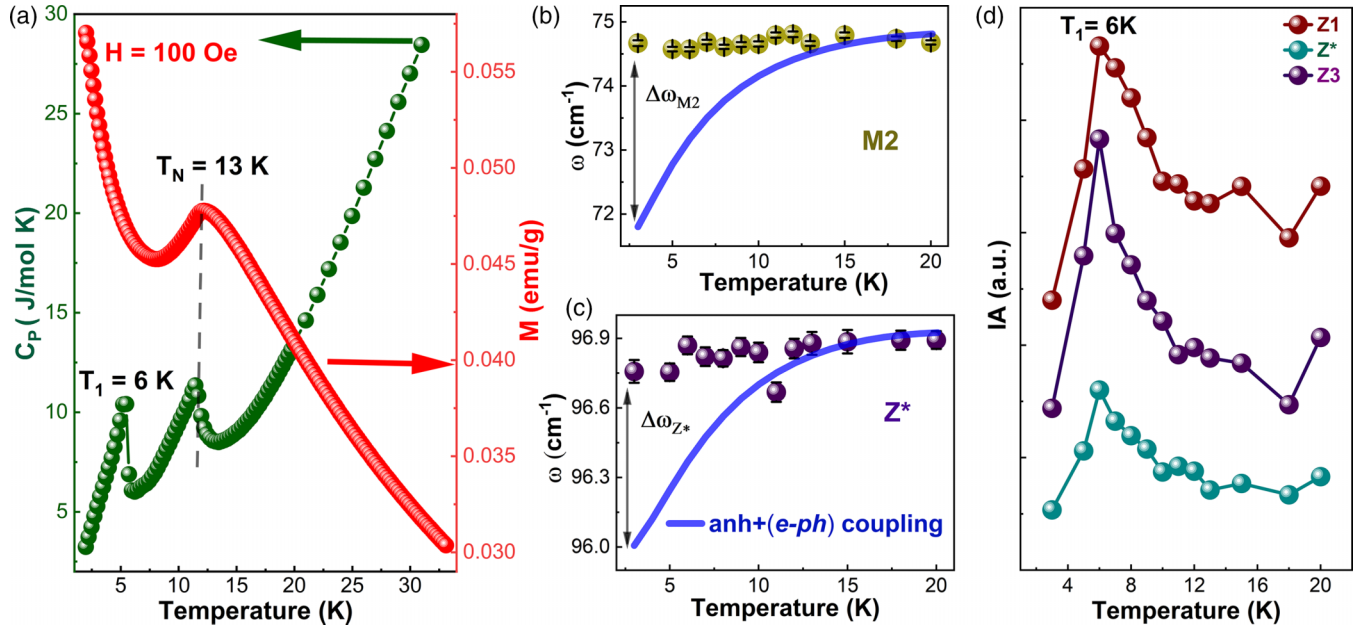

FIG. 4. (a) Low temperature $C_p(T)$ and $M(T)$ of bulk $GdTe_3$. The $C_p(T)$ data suggest two transitions, ∼6 K and ∼13 K. The magnified view of $\omega(T)$ of (b) $M2$, and (c) Z^* in the temperature range 3–20 K. Here, solid blue line is the fitting with the involvement of *e-ph* coupling in anharmonicity. (d) The IA(T) of $Z1$, Z^*, and $Z3$ in the range 3–20 K.

S_i and S_j are nearest neighbors spins at ith and jth sites, respectively, and λ_{s-ph} is the coefficient of spin-phonon (*s-ph)* coupling [30]. To emphasize the contribution of *s-ph* coupling via phonon renormalization, the $\omega(T)$ has been analyzed using the involvement of *e-ph* coupling in the equation of cubic anharmonicity: $\omega(T) = \omega_0 + \Delta\omega_{anh} + \Delta\omega_{e-ph}$, where ω_0 is the ω at zero temperature [31]. The second term, $\Delta\omega_{anh} = -\alpha g(T, \omega_0)$; where $g(T, \omega_0) = 1 + 2/(e^{\hbar\omega_0/2k_BT} - 1)$, k_B is the Boltzmann constant, and α is a constant describing the phonon-phonon strength. The third term $\Delta\omega_{e-ph} = \beta h(T, \omega_0)$, where $h(T, \omega_0) = [f(-\frac{\hbar\omega_0}{2}) - f(\frac{\hbar\omega_0}{2})]$, $f(x)$ represents the Fermi function, and β is the constant [32,33]. The Fano line shape of Raman modes (Fig. S5 of the SM [27]) indicates the existence of *e-ph* coupling, which varies with the temperature. Hence, it is reasonable that the $\omega(T)$ of all modes can be analyzed using the linear combination of anharmonicity and *e-ph* coupling. The $\omega(T)$ of $M1$, $M2$, $Z1$, Z^*, and $Z3$ are well fitted above $T \sim 13$ K, as shown in Fig. S6 of the SM, and extracted parameters are mentioned in Table SIII of the SM [27]. The higher value of $\beta \sim 5.32$ (especially of $M2$) is interpreted as the *e-ph* coupling constant, which is in line with the observation by Dutta *et al.* using the modified mean-field model [25,34]. Interestingly, the $\omega(T)$ shows a deviation from the fitted data, at $T < 13$ K [Fig. S6(b) of the SM [27]], which is significant in the $\omega(T)$ of $M2$ [Fig. 4(b)] and Z^* [Fig. 4(c)], indicating the *s-ph* coupling owing to the AFM ordering. In $GdTe_3$, Gd in +3 electronic states is the only magnetic ion, therefore $S = 7/2$ will give the approximate value of $\langle S_i \cdot S_j \rangle \sim S^2$ and is estimated to be ∼12.25. Using the phonon renormalization, the λ_{s-ph} is estimated and found in the range $\sim 0.02 - 0.23$. Comparing all modes, the $M2$ (∼0.23) and Z^* (∼0.06) have significant λ_{s-ph} values (Table SIV of the SM [27]). Modes $M2$ and Z^* primarily involve the vibration of Gd atoms in the insulating GdTe slab (here Te is silent), while the Te atoms of the conducting sheet participate in vibrations [Fig. 2(c)].

Further, the IA(T) of the $Z1$, Z^*, and $Z3$ show a sudden rise from 3 to 6 K, followed by decrease below ∼13 K, as shown in Fig. 4(d). Above 13 K, there are minor changes up to ∼150 K, then a decrease with the increase in temperature (Fig. S7 of the SM [27]). In the literature, the striped AFM phase has been discussed below 7 K [35]. However, the IA(T) around 6 K may be inferred from the possible formation of stable CCDW [7]. In general, the CCDW state occurs due to the complete opening of a gap that decreases in the electronic density at E_F [7]. Hence, from the analysis of the data, the existence of both magnetic and structural ordering can lead to a competition between the AFM and CCDW state in $GdTe_3$.

Overall, the complete phase diagram from the $\omega(T)$ of Z1 corresponds to different magnetic and structural ordering as shown in Fig. 5. Different regions have been classified such

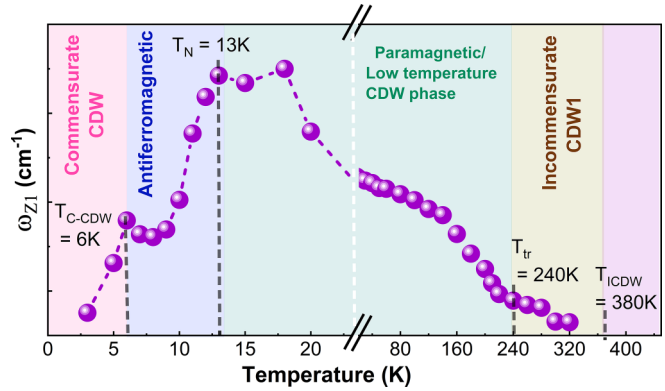

FIG. 5. The phase diagram based on the $\omega(T)$ of $Z1$ and various transition regions have been identified corresponding to T_{ICDW}, T_{tr}, T_N, T_{CCDW}.

as (i) $T > T_{\mathrm{ICDW}}$ (purple region), (ii) ICDW phase below $T_{\mathrm{ICDW}} \sim 380$ K (brown region), (iii) ordered phase below $T_{\mathrm{tr}} \sim 240$ K (green region), (iv) AFM phase below $T_N \sim 13$ K (blue region), and (v) CCDW phase below $T_{\mathrm{CCDW}} \sim 6$ K (pink region). The evidence of multiple CDW order and AFM indicates the significant role of *e-ph* and *s-ph* coupling, which can be addressed by experimental data within the error limit of instruments. Our low temperature Raman study with magnetic measurement suggests that both electronic and magnetic ordering can be correlated with each other and have a strong effect on the phonon dynamics of ZF and AMP modes.

IV. CONCLUSION

In summary, our investigation into the multiple CDW transitions and their correlation with magnetism in $GdTe_3$ has been conducted by examining the phonon dynamics of CDW-coupled amplitude and zone-folded modes using low-temperature Raman spectroscopy supported by heat capacity and magnetization studies. We are proposing a possibility of another ordering (T_{tr}) at ∼240 K, from the existence of Z^* in the low temperature region and the anomalous variation of $\omega(T)$ and IA(T) of amplitude modes. We have estimated and quantified the electron-spin phonon coupling strengths, with $\lambda_{\mathrm{s-ph}} \sim 0.234$, using phonon renormalization (specifically, of $M2$). Additionally, we present a comprehensive phase diagram encompassing the temperature regions (T_{ICDW}, T_{tr}, T_N, T_{CCDW}) of multiple CDW and magnetic phase in $GdTe_3$.

ACKNOWLEDGMENTS

D.R. and A.S. would like to acknowledge IIT Mandi for the research facilities. D.N. acknowledges CSIR for fellowship (09/1020(0139)/2018-EMR-II). K.B. acknowledges financial support from Swarna Jayanti fellowship grant, Science and Engineering Research Board (SERB, DST) (SB/SJF/2019-20/06), India.

[1] B. Keimer and J. E. Moore, The physics of quantum materials, Nat. Phys. **13**, 1045 (2017).

[2] S. Paul, D. Negi, S. Talukdar, S. Karak, S. Badola, B. Poojitha, M. Mandal, S. Marik, R. P. Singh, N. Pistawala *et al.*, Tuning the robust magnetic properties in MPS_3 (M = Mn, Fe, and Ni) by proximity-induced Dzyaloshinskii-Moriya interactions, Phys. Rev. B **109**, 085136 (2024).

[3] X. Teng, J. S. Oh, H. Tan, L. Chen, J. Huang, B. Gao, J.-X. Yin, J.-H. Chu, M. Hashimoto, D. Lu *et al.*, Magnetism and charge density wave order in kagome FeGe, Nat. Phys. **19**, 814 (2023).

[4] G. Grüner, The dynamics of charge-density waves, Rev. Mod. Phys. **60**, 1129 (1988).

[5] V. Brouet, W. L. Yang, X. J. Zhou, Z. Hussain, R. G. Moore, R. He, D. H. Lu, Z. X. Shen, J. Laverock, S. B. Dugdale *et al.*, Angle-resolved photoemission study of the evolution of band structure and charge density wave properties in RTe_3 (R = La, Ce, Sm, Gd, Tb, and Dy), Phys. Rev. B **77**, 235104 (2008).

[6] M. Lavagnini, H. M. Eiter, L. Tassini, B. Muschler, R. Hackl, R. Monnier, J. H. Chu, I. R. Fisher, and L. Degiorgi, Raman scattering evidence for a cascade evolution of the charge-density-wave collective amplitude mode, Phys. Rev. B **81**, 081101(R) (2010).

[7] J. Pandey and A. Soni, Electron-phonon interactions and two-phonon modes associated with charge density wave in single crystalline VSe_2, Phys. Rev. Res. **2**, 033118 (2020).

[8] J. Laverock, S. B. Dugdale, Z. Major, M. A. Alam, N. Ru, I. R. Fisher, G. Santi, and E. Bruno, Fermi surface nesting and charge-density wave formation in rare-earth tritellurides, Phys. Rev. B **71**, 085114 (2005).

[9] D. Rawat, A. Thomas, A. P. Singh Rana, C. Bera, and A. Soni, Symmetry breaking and structural instability in ultrathin $2H$-TaS_2 across the charge density wave transition, Phys. Rev. B **109**, 155411 (2024).

[10] J. Wilson, F. Di Salvo, and S. Mahajan, Charge-density waves in metallic, layered, transition-metal dichalcogenides, Phys. Rev. Lett. **32**, 882 (1974).

[11] K. Rossnagel, On the origin of charge-density waves in select layered transition-metal dichalcogenides, J. Phys.: Condens. Matter **23**, 213001 (2011).

[12] M. Klein, Theory of two-phonon Raman scattering in transition metals and compounds, Phys. Rev. B **24**, 4208 (1981).

[13] Y. Iyeiri, T. Okumura, C. Michioka, and K. Suzuki, Magnetic properties of rare-earth metal tritellurides RTe_3 (R = Ce, Pr, Nd, Gd, Dy), Phys. Rev. B **67**, 144417 (2003).

[14] F. Qin, S. Li, Z. Du, C. Wang, W. Zhang, D. Yu, H.-Z. Lu, and X. C. Xie, Theory for the charge-density-wave mechanism of 3D quantum Hall effect, Phys. Rev. Lett. **125**, 206601 (2020).

[15] K. Yumigeta, Y. Qin, H. Li, M. Blei, Y. Attarde, C. Kopas, and S. Tongay, Advances in rare-earth tritelluride quantum materials: Structure, properties, and synthesis, Adv. Sci. News **8**, 2004762 (2021).

[16] A. Kogar, A. Zong, P. E. Dolgirev, X. Shen, J. Straquadine, Y.-Q. Bie, X. Wang, T. Rohwer, I. C. Tung, Y. Yang *et al.*, Light-induced charge density wave in $LaTe_3$, Nat. Phys. **16**, 159 (2020).

[17] V. Brouet, W. L. Yang, X. J. Zhou, Z. Hussain, N. Ru, K. Y. Shin, I. R. Fisher, and Z. X. Shen, Fermi surface reconstruction in the CDW state of $CeTe_3$ observed by photoemission, Phys. Rev. Lett. **93**, 126405 (2004).

[18] M. Lavagnini, M. Baldini, A. Sacchetti, D. Di Castro, B. Delley, R. Monnier, J. H. Chu, N. Ru, I. R. Fisher, P. Postorino *et al.*, Evidence for coupling between charge density waves and phonons in two-dimensional rare-earth tritellurides, Phys. Rev. B **78**, 201101(R) (2008).

[19] N. Lazarević, Z. V. Popović, R. Hu, and C. Petrovic, Evidence of coupling between phonons and charge-density waves in $ErTe_3$, Phys. Rev. B **83**, 024302 (2011).

[20] J. S. Liu, S. C. Huan, Z. H. Liu, W. L. Liu, Z. T. Liu, X. L. Lu, Z. Huang, Z. C. Jiang, X. Wang, N. Yu *et al.*, Electronic structure of the high-mobility two-dimensional antiferromagnetic metal $GdTe_3$, Phys. Rev. Mater. **4**, 114005 (2020).

[21] B. F. Hu, B. Cheng, R. H. Yuan, T. Dong, and N. L. Wang, Coexistence and competition of multiple charge-density-wave

orders in rare-earth tritellurides, Phys. Rev. B **90**, 085105 (2014).

[22] Y. Chen, P. Wang, M. Wu, J. Ma, S. Wen, X. Wu, G. Li, Y. Zhao, K. Wang, L. Zhang *et al.*, Raman spectra and dimensional effect on the charge density wave transition in $GdTe_3$, Appl. Phys. Lett. **115**, 151905 (2019).

[23] Q. Guo, D. Bao, L. J. Zhao, and S. Ebisu, Novel magnetic behavior of antiferromagnetic $GdTe_3$ induced by magnetic field, Physica B: Cond. Matter **617**, 413153 (2021).

[24] D. A. Zocco, J. J. Hamlin, K. Grube, J. H. Chu, H. H. Kuo, I. R. Fisher, and M. B. Maple, Pressure dependence of the charge-density-wave and superconducting states in $GdTe_3$, $TbTe_3$, and $DyTe_3$, Phys. Rev. B **91**, 205114 (2015).

[25] P. Dutta, S. Chandra, I. Maria, K. Debnath, D. Rawat, A. Soni, U. V. Waghmare, and K. Biswas, Lattice instability induced concerted structural distortion in charged and van der Waals layered $GdTe_3$, Adv. Funct. Mater. **34**, 2312663 (2023).

[26] J. Zhang, Z. Peng, A. Soni, Y. Zhao, Y. Xiong, B. Peng, J. Wang, M. S. Dresselhaus, and Q. Xiong, Raman spectroscopy of few-quintuple layer topological insulator Bi_2Se_3 nanoplatelets, Nano Lett. **11**, 2407 (2011).

[27] See Supplemental Material at http://link.aps.org/supplemental/10.1103/PhysRevB.110.075155 for the additional Raman, heat capacity, and magnetic data complementary to the main text.

[28] S. Saha, S. Prusty, S. Singh, R. Suryanarayanan, A. Revcolevschi, and A. Sood, Pyrochlore "dynamic spin-ice" $Pr_2Sn_2O_7$ and monoclinic $Pr_2Ti_2O_7$: A comparative temperature-dependent Raman study, J. Solid State Chem. **184**, 2204 (2011).

[29] D. V. West, I. D. Posen, Q. Huang, H. W. Zandbergen, T. M. McQueen, and R. J. Cava, $PbMn(SO_4)_2$: A new chiral antiferromagnet, J. Solid State Chem. **182**, 2461 (2009).

[30] A. Ghosh, M. Palit, S. Maity, V. Dwij, S. Rana, and S. Datta, Spin-phonon coupling and magnon scattering in few-layer antiferromagnetic $FePS_3$, Phys. Rev. B **103**, 064431 (2021).

[31] M. Kuiri, S. Das, D. Muthu, A. Das, and A. Sood, Thickness dependent transition from the 1T′ to Weyl semimetal phase in ultrathin $MoTe_2$: Electrical transport, noise and Raman studies, Nanoscale **12**, 8371 (2020).

[32] J. Pandey, D. Ghoshal, D. Dey, T. Gupta, A. Taraphder, N. Koratkar, and A. Soni, Local ferroelectric polarization in antiferroelectric chalcogenide perovskite $BaZrS_3$ thin films, Phys. Rev. B **102**, 205308 (2020).

[33] N. K. Singh, D. Rawat, D. Dey, A. Elsukova, P. O. Å. Persson, P. Eklund, A. Taraphder, and A. Soni, Electron-phonon coupling and quantum correction to topological magnetoconductivity in Bi_2GeTe_4, Phys. Rev. B **105**, 045134 (2022).

[34] S. Wang, X. Chen, C. An, Y. Zhou, M. Zhang, Y. Zhou, Y. Han, and Z. Yang, Observation of room-temperature amplitude mode in quasi-one-dimensional charge-density-wave material CuTe, Appl. Phys. Lett. **120**, 151902 (2022).

[35] A. Raghavan, M. Romanelli, J. May-Mann, A. Aishwarya, L. Aggarwal, A. G. Singh, M. D. Bachmann, L. M. Schoop, E. Fradkin, I. R. Fisher *et al.*, Atomic-scale visualization of a cascade of magnetic orders in the layered antiferromagnet $GdTe_3$, npj Quantum Mater. **9**, 47 (2024).